RSC Advances

ROYAL SOCIETY OF CHEMISTRY

www.rsc.org/advances

Physicochemical Interface Effect in Cu_2O-ZnO Heterojunction on Photocurrent Spectrum

Kiryung Eom,[a], Seunghwan Kim,[b] Dongyoon Lee,[b] Hyungtak Seo[a,*]

[a]Department of Energy Systems Research and Department of Materials Science & Engineering, Ajou University, Suwon 443-739, Republic of Korea

[b]Gyeonggi Science High School, Suwon 440-800, Republic of Korea

Abstract

This study reports the effect of oxide heterojunction solar cell (HSC) arrangement on the solar photocurrent spectra and physical correlation to the interfacial band electronic structure. Based on *p*-Cu_2O/*n*-ZnO oxide junction, two types of stack arrangement were prepared to observe the solar photocurrent spectral change: FTO/Cu_2O/ZnO/Al and FTO/ZnO/Cu_2O/Al structure. As the photovoltaic cell structure, FTO was utilized for *p*-type electrode, Cu_2O for *p*-type semiconductor, ZnO for n-type semiconductor and Al n-type electrode. The HSC characteristics were characterized by ultraviolet-visible spectroscopy, X-ray photoelectron spectroscopy (XPS), diode current-voltage measurement, and finally, incident photon-to-current efficiency (IPCE), respectively. As a result, the IPCE spectra of HSC were large affected by (1) the band gap of first layer semiconductor which has the first light incidence regardless of the bandgap energy and (2) the interfacial electronic bandoffset values in each stack. Therefore, this result offers a possible mechanism that HSC consisting of FTO/Cu_2O/ZnO stack shows better IPCE response than FTO/ZnO/Cu_2O stack in the view of electronic band-alignment.

Keywords : heterojunction solar cell, Cu_2O, ZnO, IPCE, band structure

*E-mail: hseo@ajou.ac.kr

1. Introduction

Researches on oxide heterojunction solar cell (HSC), consists of a p-n junction with different bandgap oxide layers have been actively performed because of its cost-effectiveness, facile manufacturing process control, and reliable material properties. These merits place the oxide HSC as the potential future solar cell, which can offer the technical solutions to meet current requirements in commercial solar cell industry such as low raw material price, low manufacturing cost, and easy mass-production process. Nevertheless, the power conversion efficiency (PCE) of oxide HSCs is much lower than Si and chalcogenide thin film solar cells. Although the merit of oxide HSC is related to abundancy of metal oxide species such as Cu-oxide and Zn-oxide, best PCE levels of oxide HSC have been reported only at 1-5 % unless using either rare-earth p- or n-type metal oxides. [1] Therefore, research activities on oxide HSC are mainly focused on the improvement of PCE level. [2, 3] Among many oxides considered for absorber layer, Cu_2O is highlighted as a p-type semiconductor with its bandgap at 2.1 eV and PCE level is theoretically expected to reach upto 17%. Since Cu_2O is non-toxic, naturally abundant, and can be fabricated and processed at the low cost, its various application to light emitting diode, gas sensors, and p-type absorber in solar cell is being studied. [4-7]

In conventional homo-junction solar cell like Si p-n junction, the interfacial properties is well predicted and modeled so that it comes with easily controllable design factors. [8-10] However, as to oxide HSCs, the interface is the most challenging part due to the significant chemical mixing of elements, non-stoichiometry, and defect/trap-site generation. In view of solar cell operation, this arises a large uncertainty about the interfacial bandoffset which determines the effective carrier separation at the junction. Although theoretical prediction was made on band-alignment model based on the previous report, the degree of precision based on such predicted models is not so high at all in the case of oxide HSC.[11] This raises the need for experimental approaches to investigate the interfacial psychochemical properties using the proper spectroscopic techniques.

In this study, we investigated the effect of interfacial properties on photon energy dependent PCE for *p*-Cu_2O/*n*-ZnO HSC by changing the stack arrangement. In typical thin film HSC cell, there are the top window layer with large bandgap n-type semiconductor and then, the absorber with small bandgap p-type semiconductor at the bottom. However, we found the significant solar photocurrent spectral change in incident photon-to-current efficiency (IPCE) as reversing the stacking order to the conventional one. In order to investigate this as focusing the interfacial chemical properties and band-alignments in both p/n and metal-semiconductor junction, spectroscopic measurements using

ultraviolet-visible (UV-vis) spectrometer and X-ray photoelectron spectroscopy (XPS) measurements were carried out. This result provides a valuable guideline for Cu_2O-based oxide HSC structure optimization based on the electronic band-alignment.

2. Experimental

The 0.7~4 ㎛ thick p-type cupric oxide, Cu_2O was fabricated on fluorine doped tin oxide (FTO) glass by electrodeposition method as applying -3 V of bias at 60℃ in pH 9 solution consisting of 0.2M copper sulfate (>99.9%, Sigma Aldrich) and 3M Lactic Acid (88~92%, Sigma Aldrich) for 40 min. [12-15] The 120 nm thick n-type ZnO was deposited by RF magnetron sputtering at the condition of preheating 10 min, pre-sputter 5 min, 300℃, and 1.00×10^{-2} Torr under Ar 10 sccm flow. In addition, the reverse layer sequence, ZnO deposition in vacuum on FTO followed by Cu_2O was also applied to minimize subcutaneous oxidation of Cu_2O led by the high temperature ZnO sputtering. For this p-n junction, Al electrode with the thickness of 50 nm and the diameter of 100 ㎛ was deposited by electron-beam deposition.

The diode I-V characteristic was evaluated by Keithley 2612 current-voltage (I-V) source meter. The photocurrent spectra as the function of wavelength (from 1200 to 300 nm) of monochromatic incident light generated by Xenon lamp onto Al electrode in HSC were measured to achieve IPCE results. The standard Si solar cell (BS-500, BUNKOUKEIKI Co., Japan) was utilized to calculate the IPCE. The crystal structures were analyzed by X-ray diffraction (XRD, UltimaⅢ, Rigaku, Japan) and the surface chemical binding state, valence band-edge state, and depth-profile were obtained by X-ray photoelectron spectroscopy (XPS, theta probe base system, Thermo Fisher Scientific Co., USA). The bandgap of each layer was determined by UV-vis spectrometer (Cary 5000, Agilent, USA) analysis.

3. Results and Discussion

The crystallinity of Cu_2O (at the thickness of 4.2 ㎛, 1.9 ㎛, and 720 ㎚) on FTO (at the thickness of 250 ㎚) glass as a function of thickness was evaluated by XRD from 20 to 50° of diffraction angle by the angle interval of 0.02° (Fig. 1a). XRD data revealed diffraction peaks of

Cu_2O corresponding to the cubic structure (JCPDS-01-071-3645, a=0.42685nm) having (110), (111), and (200) plane at 29.66°, 36.54°, and 42.33° respectively. The 1.9 ㎛ thick sample shows the strongest XRD peaks among samples even than the thickest (4.2 ㎛) sample, indicating the crystallinity does not scale with the film thickness as in the film deposited by vacuum deposition. Based on the XRD peak intensity, the preferential crystal plane of Cu_2O is also changed from (200) for 720 nm and 1.9 ㎛ thick films to (111) for 4.2 ㎛ thick film. Upon fabrication of diodes, the best diode results were obtained at 720 nm thick Cu_2O film while diodes with other Cu_2O films revealed the poor performance (not shown here). This indicates that the bulk crystallinity of Cu_2O film is not a decisive but only partial effect to control the diode characteristic. We rather consider that interface of Cu_2O/ZnO is more relevant to the diode property. SEM data in Fig. 1(b) and (c) reveal the cross-sectional morphology of FTO/ZnO /Cu_2O and FTO/Cu_2O/ZnO stack respectively. In order to distinguish each layer easily, the target thickness of each layer was set to 200 nm for ZnO and 500 nm for Cu_2O but the interface formation leads to variation in the resulted thickness from SEM images. Each layer was formed as a continuous film and energy dispersive spectroscopy analysis on the specific spots identified the distinctive Cu and Zn in CuO and ZnO layer respectively as shown in atomic % plots of Fig 1(b) and (c).

UV-vis spectroscopy analysis was performed to achieve the optical bandgap to be used for the electronic band structure model by taking absorbance and transmission data (Fig. 2). In Fig. 2 (a) and (b), Cu_2O has the high absorbance at 300-500 nm of wavelength, corresponding to UV and all visible range and this confirms that Cu_2O has a clear advantage to absorb the incident light and produce photo-carriers in the visible range. In Fig. 2 (c) and (d), ZnO revealed the strong absorbance at < 400 nm of wavelength and its high transparency at > 80 % in the visible range, which makes ZnO the ideal material for the window layer of solar cell. The optical bandgap from UV-vis absorbance data was extracted by Tauc plot in Fig. 3. Tauc plots ($(\alpha h\nu)^{\frac{1}{n}}$ vs. $h\nu$) curves were plotted for different n (n= 1/2, in the case of direct band gap) values, α is the absorption coefficient calculated from absorption spectra and photon energy. [16] The direct bandgaps of Cu_2O and ZnO were 1.4 and 3.2 eV respectively. [17-19] However, the typical Cu_2O optical bandgap is ~ 2.1 eV and this bandgap difference is related to the formation of CuO at the electrodeposited Cu_2O surface, which rapidly occurs in air ambient. Indeed, the absorbance data in Fig. 2(a) shows the marked absorbance in the wavelength down to 1100 nm, which is due to light absorption in the surface CuO subphase. [20] The effect of stack arrangement of Cu_2O and ZnO layers on the optical property was investigated by UV/vis

analysis in Fig. 4. The stack of FTO/Cu_2O/ZnO/Al shows the lower absorbance in the range of 600-1000 nm than the reverse stack arrangement (FTO/ZnO/Cu_2O/Al) but with no difference in the range of 300-500 nm, which is the high absorbance band. Therefore, it is deduce from Fig. 4 that the stacking arrangement has an outstanding impact on degree of CuO phase formation on Cu_2O surface, leading to absorbance at 500-1100 nm but no effect on the strong absorption region due to ZnO and Cu_2O phase.

I-V results in Fig. 5 shows the p/n diode characteristics of differently stacked oxide junctions. Both junctions revealed the regular diode property with the asymmetric I-V behavior with bias polarity. However, the bias polarity with forward current is different depending on the junction type; – bias for ZnO/Cu_2O (n/p) junction (Fig. 5(a)) and + bias for Cu_2O/ZnO (p/n) junction (Fig. 5(b)). It is noted that the diode rectification of ZnO/Cu_2O is inferior to Cu_2O/ZnO since CuO subphase formed on Cu_2O generates the additional energy barriers for charge transport. [21, 22] Under the dark-current condition, the rectification factor of each diode at ± 5V is 2 for ZnO/Cu_2O and 30 for Cu_2O/ZnO stacks. The photo-current is clearly observed in both diodes upon the light exposure condition and particularly, the ratio of photo-current/dark-current for Cu_2O/ZnO is > ~10^3, offering a good visible photo-response performance. The repeated I-V curves with 10 cyclic sweeps and time-dependent transient photo-current traces under the continuous bias at 2V are shown in Fig. 5(c) and (d) for each stack. It turns out that Cu_2O/ZnO stack has an outstanding dark-current baseline drift compared to ZnO/Cu_2O without (1) a noticeable change in the net photo-current level and (2) no residual lag in time-dependent photo-current transition. This suggests that FTO/Cu_2O/ZnO stack has a high number of non-photoactive charge trap sites, which is considered to be intrinsically formed at FTO/Cu_2O interface, which is the different interface from FTO/ZnO interface in FTO/ZnO/Cu_2O stack.

Figure 6 shows IPCE spectra to investigate the spectral response of photocurrent as changing stack arrangement. In IPCE spectra for Cu_2O/ZnO junction, three distinctive photo-current bands are observed at <400, 400-600, and 900-1200 nm of wavelnegth. Based on optical absorption data in Fig. 4, each band corresponds to the photo-carrier generation in ZnO (< 400 nm) and Cu_2O (400-600, 900-1200 nm). However, ZnO/Cu_2O junction shows the overall low IPCE spectra except the wavelength range at 1000-1200 nm in spite that the optical absorption in ZnO/Cu_2O is almost same as Cu_2O/ZnO and its optical absorption in the long wavelength range at 1000-1200 nm is even higher than Cu_2O/ZnO junction. The relatively high IPCE at 1000-1200 nm in ZnO/Cu_2O junction is

regarded due to CuO subphase, the bandgap of which is 1036 nm or 1.2 eV. [15, 21, 22] The lower IPCE in ZnO/Cu_2O junction compared to Cu_2O/ZnO junction over the most wavelength range indicates that the electronic band alignment affected by CuO subphase on Cu_2O plays a crucial role in IPCE. Therefore, XPS analysis was performed to evaluate the band alignment structure of each junction. PCEs of Cu_2O/ZnO HSC are reported to be 0.1 to 3 %.[2, 3, 14, 23] The PCE level of Cu_2O/ZnO HSC in this study is ~ 0.1%, requiring more optimization. Nevertheless, IPCE reaching 25% between 800-1200 nm of wavelength is not reported in other works[1, 3, 24] so that can be considered to compensate a low PCE level in the long wavelength range.

Fig. 7 (a) and (b) represents XPS depth profiles (atomic elemental percent as a function of Ar sputtering time) for (1) FTO/Cu_2O and (2) Cu_2O/ZnO respectively. For sample (1), the FTO-Cu_2O interfacial band alignment and CuO band structures are determined and for sample (2), the Cu_2O/ZnO interfacial band alignment is obtained. The Ar sputtering condition was 0.2 nm/sec (referenced to SiO_2) and the sputtering raster area was 1 mm^2. In Fig. 7(a) for FTO/Cu_2O, the position at 0 sec of sputter time (or etch time) corresponds to Cu_2O top surface and 150 sec of sputter time is considered as FTO with a reduction of Cu-2p atomic percent. In Fig. 7(b) for Cu_2O/ZnO, the position at 0 sec of sputter time corresponds to ZnO top surface with high atomic percent of Zn-2p, at 300-400 sec is the interfacial region, and at >500 is considered as Cu_2O with the rapid increase of Cu-2p atomic percent. From the XPS depth profile, the elemental information along the depth position is identified, Cu-2p binding states were analyzed at the specific points at the surface and bulk for each sample. As shown in Fig. 7(c), at the Cu_2O top surface in sample 1 (0 sec of sputter time), CuO (933.4 eV) and $Cu(OH)_2$ (934.7 eV) binding states are resolved and satellite peaks of CuO (Cu(2+)) appear at 943.8 and 941.3 eV. This bond character clearly indicates that Cu_2O surface in sample 1 has CuO subphase. In the bulk region of sample 1 (150 sec of sputter time), only Cu_2O binding state (932.6 eV) is resolved without CuO subphase features (Fig. 7c). On the other hand, sample 2 revealed only Cu_2O binding state (932.6 eV) in both surface and bulk region without any CuO-associated binding states and satellite peaks (Fig. 7d). This confirms the formation of subcutaneous CuO-free Cu_2O/ZnO interface in sample 2 due to the deposition of ZnO in vacuum onto CuO in the sputtering chamber without air exposure.

At the specific point of sample, valence band maximum (VBM) as referenced to the Fermi energy level (E_F) level was extracted by inspecting onset energy of the valence band edge XPS spectra. VBMs at the ZnO bulk (30 sec of sputter time in Fig. 7(b)) and at the Cu_2O bulk (1170 sec of sputter

time) are 1.75 eV (Fig. 8(a)) and 0.18 eV (Fig. 8 (b)) respectively. Using similar experimental approach combined with optical bandgap data in Fig. 3 and reference data for metal work functions and electron affinities [25-29], band alignments containing conduction band offset (CBO) and valence band offset (VBO) as referenced to E_F level are calculated for FTO/ZnO, FTO/Cu_2O, CuO/Al, and ZnO/Al interfaces to construct the band alignment model in Fig. 8 (c) and (d) for FTO/Cu_2O/ZnO/Al (i.e., stack 1) and FTO/ZnO/Cu_2O/Al (i.e., stack 2) arrangements respectively. First, when the semiconductor work function is larger than metal electrodes at the interface of electrodes and the semiconductor junction such as FTO/ZnO and Al/Cu_2O, calculation of the barrier height (V_o) of the Schottky diode is done using Eg. (1). [30, 31] This gives the Schottky barrier at each interface. (0.04eV at the interface between FTO/Cu_2O, 1.6eV at Al/ZnO, 0.59eV at Al/CuO)

$$\phi_s - \phi_m = V_o \ \ (\phi_m < \phi_s) \quad (1),$$

Where Φ_s is the work function of semiconductor and Φ_m is the work function of metal.

Also, from the theory introduced by Kraut [32], the VBO (ΔE_v) can be calculated by Eq. (2) and (3) as following:

$$\Delta E_v = E_{VB}^B - E_{VB}^A + \left[\left(E_{CL}^A - E_{CL}^{A/B}\right) + \left(E_{CL}^{B/A} - E_{CL}^B\right)\right] \quad (2),$$

$$\Delta E_c = E_g^B - E_g^A + \Delta E_v \quad (3),$$

Where E_{VB}^B and E_{VB}^A are bulk A and B materials core-level energies and $E_{CL}^{A/B}$ and $E_{CL}^{B/A}$ are the same core-level energies of A and B at the interface. The CBO (ΔE_c) can then be calculated using the Eq. (2) and (3). [32-34] In our experiment setup, since the light incidence occurred onto Al electrode, CuO subphase present at the surface of Cu_2O in stack 2 first absorbs the high portion of light due to its low bandgap. The major optical absorption of CuO subphase is present in stack 2 so that the effective photo-carrier generation in Cu_2O, inserted as absorber, is substantially reduced. In addition, the hole transport in stack 2 is rather reduced in the both direction of Cu_2O→CuO (VBO at 0. 22eV) and Cu_2O→ZnO (VBO at 1.49 eV) as limiting hole photo-current (Fig. 8(d)). In stack 2, the direction of electron transport can occur both directions; (1) from Cu_2O to FTO and (2) CuO to Al so that it may lead to the electron-hole recombination in CuO. On the other hand, in stack 1 (Fig. 8(c)), the incident light is mostly absorbed by Cu_2O without perturbation of CuO subphase since ZnO has the large UV-range bandgap at 3.2 eV. Furthermore, electron transport form Cu_2O to Al via ZnO is drifted by the downward band alignment without CBO and hole transport from Cu_2O to FTO is also

facile with VBO at 0.26 eV. As a consequence, the band-alignment model explains electronic band features about the light absorption for photo-carrier generation, separation, and transport with experimentally defined CBO and VBO values in each HSC arrangement. 1

4. Conclusions

This article reports the spectral change in solar photocurrent upon altering arrangement of Cu_2O and ZnO layer in oxide HSC. Based on XPS analysis, top surface Cu_2O has subcutaneous CuO subphase layer upon air ambient exposure in the case of FTO/ZnO/Cu_2O arrangement, which diminishes the light absorption in Cu_2O because of the high light absorption in the small bandgap (1.4 eV) subcutaneous CuO surface layer. As a result, FTO/ZnO/Cu_2O/Al HSC stack has much lower IPCE over the entire wavelength than FTO/Cu_2O/ZnO/Al stack. The band-alignment analysis, combining VB-edge XPS spectra (for VBM), UV-vis data (for optical bandgap), and reported work function and electron affinity values, yields the full electronic band-structure and alignment for each stack. From this, the first layer receiving incident light is most important for solar photocurrent spectra since it decisively affects IPCE by altering the dominant light absorption features in the stack and VBO and CBO in band electronic structure for charge transport. The CuO subphase in ZnO/Cu_2O stack is negative for all these respects but CuO/ZnO stack has the clear advantage in band-alignment with no CBO and very small VBO values. This study therefore highlights the importance of band-alignment characterization to clarify the photo-current mechanism in oxide HSC based on experimental analysis for efficiency optimization.

5. Acknowledgement

This work was supported by the National Research Foundation (NRF) (the Basic Science Program (NRF-2015R1A2A2A01003790 and NRF-2009-0094046) and by C1 Gas Refinery Program (2015M3D3A1A01064899) funded by Ministry of Education and Ministry of Science, ICT, and Future Planning, Republic of Korea. K. Uhm and S. Kim and equally contributed to this work.

6. References

1. Y. Ievskaya, R. L. Z. Hoye, A. Sadhanala, K. P. Musselman and J. L. MacManus-Driscoll,

Solar Energy Materials and Solar Cells, 2015, **135**, 43-48.
2. A. Mittiga, E. Salza, F. Sarto, M. Tucci and R. Vasanthi, *Applied Physics Letters*, 2006, **88**, 163502.
3. K. P. Musselman, A. Wisnet, D. C. Iza, H. C. Hesse, C. Scheu, J. L. MacManus-Driscoll and L. Schmidt-Mende, *Adv Mater*, 2010, **22**, E254-E258.
4. Y. Y. Kim, C. H. An, H. K. Cho, J. H. Kim, H. S. Lee, E. S. Jung and H. S. Kim, *Thin Solid Films*, 2008, **516**, 5602-5606.
5. C. Malerba, F. Biccari, C. Leonor Azanza Ricardo, M. D'Incau, P. Scardi and A. Mittiga, *Solar Energy Materials and Solar Cells*, 2011, **95**, 2848-2854.
6. K. Matsuzaki, K. Nomura, H. Yanagi, T. Kamiya, M. Hirano and H. Hosono, *Applied Physics Letters*, 2008, **93**, 202107.
7. S. T. Shishiyanu, T. S. Shishiyanu and O. I. Lupan, *Sensors and Actuators B: Chemical*, 2006, **113**, 468-476.
8. L. Y. Isseroff and E. A. Carter, *Chemistry of Materials*, 2013, **25**, 253-265.
9. L. Papadimitriou, C. A. Dimitriadis and L. Dozsa, *Solid-State Electronics*, 1988, **31**, 1477-1482.
10. O. Lupan, S. Shishiyanu, V. Ursaki, H. Khallaf, L. Chow, T. Shishiyanu, V. Sontea, E. Monaico and S. Railean, *Solar Energy Materials and Solar Cells*, 2009, **93**, 1417-1422.
11. S. Calnan, *Coatings*, 2014, **4**, 162.
12. V. Georgieva and M. Ristov, *Solar Energy Materials and Solar Cells*, 2002, **73**, 67-73.
13. W. Septina, S. Ikeda, M. A. Khan, T. Hirai, T. Harada, M. Matsumura and L. M. Peter, *Electrochimica Acta*, 2011, **56**, 4882-4888.
14. S. W. Lee, Y. S. Lee, J. Heo, S. C. Siah, D. Chua, R. E. Brandt, S. B. Kim, J. P. Mailoa, T. Buonassisi and R. G. Gordon, *Advanced Energy Materials*, 2014, **4**, n/a-n/a.
15. P. E. de Jongh, D. Vanmaekelbergh and J. J. Kelly, *Chemistry of Materials*, 1999, **11**, 3512-3517.
16. Y. Nakano, S. Saeki and T. Morikawa, *Applied Physics Letters*, 2009, **94**, 22111.
17. Y. Nakano, S. Saeki and T. Morikawa, *Applied Physics Letters*, 2009, **94**, 022111.
18. J. Mass, P. Bhattacharya and R. S. Katiyar, *Materials Science and Engineering: B*, 2003, **103**, 9-15.
19. G. Kaur, A. Mitra and K. L. Yadav, *Progress in Natural Science: Materials International*, 2015, **25**, 12-21.
20. B. Kramm, A. Laufer, D. Reppin, A. Kronenberger, P. Hering, A. Polity and B. K. Meyer, *Applied Physics Letters*, 2012, **100**, 094102.
21. S. S. Wilson, J. P. Bosco, Y. Tolstova, D. O. Scanlon, G. W. Watson and H. A. Atwater, *Energy & Environmental Science*, 2014, **7**, 3606-3610.
22. R. E. Brandt, M. Young, H. H. Park, A. Dameron, D. Chua, Y. S. Lee, G. Teeter, R. G. Gordon and T. Buonassisi, 2014.
23. I. Masanobu, S. Tsutomu, M. Ko-Taro, I. Yuya, I. Minoru and T. Akimasa, *Journal of Physics D: Applied Physics*, 2007, **40**, 3326.
24. A. S. Zoolfakar, R. A. Rani, A. J. Morfa, S. Balendhran, A. P. O'Mullane, S. Zhuiykov and K. Kalantar-zadeh, *J Mater Chem*, 2012, **22**, 21767-21775.
25. I. Mora-Sero, L. Bertoluzzi, V. Gonzalez-Pedro, S. Gimenez, F. Fabregat-Santiago, K. W. Kemp, E. H. Sargent and J. Bisquert, *Nat Commun*, 2013, **4**.
26. M. Uda, A. Nakamura, T. Yamamoto and Y. Fujimoto, *Journal of electron spectroscopy and related phenomena*, 1998, **88**, 643-648.
27. A. Zainelabdin, S. Zaman, G. Amin, O. Nur and M. Willander, *Applied Physics A*, 2012, **108**, 921-928.

28. A. Mittiga, F. Biccari and C. Malerba, *Thin Solid Films*, 2009, **517**, 2469-2472.
29. K. Jacobi, G. Zwicker and A. Gutmann, *Surface Science*, 1984, **141**, 109-125.
30. A. M. Cowley and S. M. Sze, *Journal of Applied Physics*, 1965, **36**, 3212-3220.
31. W. Mönch, *Surface Science*, 1994, **299**, 928-944.
32. E. Kraut, R. Grant, J. Waldrop and S. Kowalczyk, *Physical Review B*, 1983, **28**, 1965.
33. W. Wei, Z. Qin, S. Fan, Z. Li, K. Shi, Q. Zhu and G. Zhang, *Nanoscale research letters*, 2012, **7**, 1-5.
34. T. D. Veal, P. King, S. Hatfield, L. R. Bailey, C. F. McConville, B. Martel, J. Moreno, E. Frayssinet, F. Semond and J. Zúñiga-Pérez, *Applied Physics Letters*, 2008, **93**, 202108.

Figures and Captions

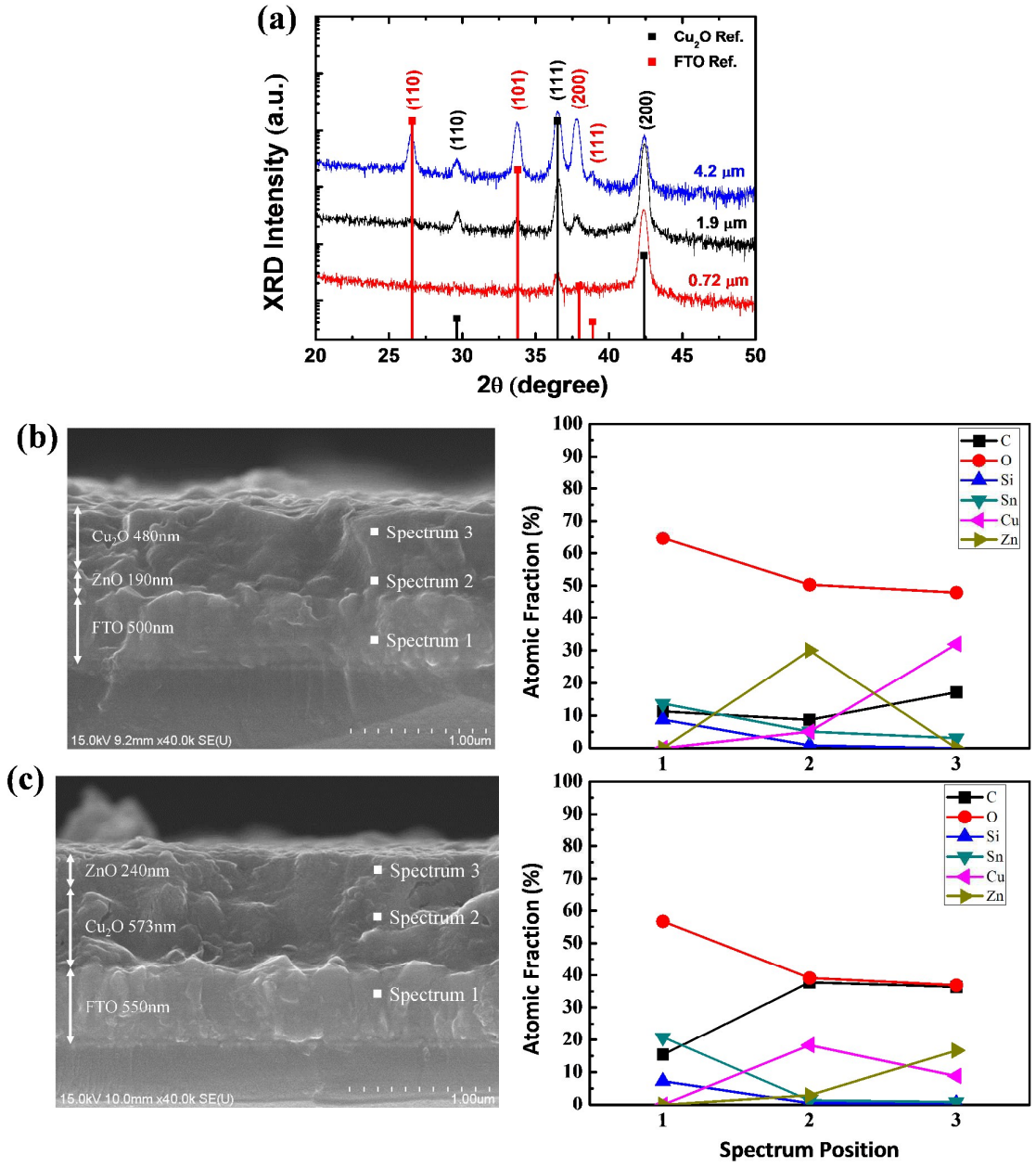

Figure 1. (a) XRD patterns of Cu_2O with different thickness (red: 720㎚, black: 1.9㎛, blue: 4.2㎛) and SEM (left) and atomic fraction (right) extracted from EDS spot analysis at each layer (spectrum

1-3) of (b) FTO/ZnO/Cu_2O and (c) FTO/Cu_2O/ZnO stacks. In XRD pattern, reference diffraction peaks from JCPDS card are shown together.

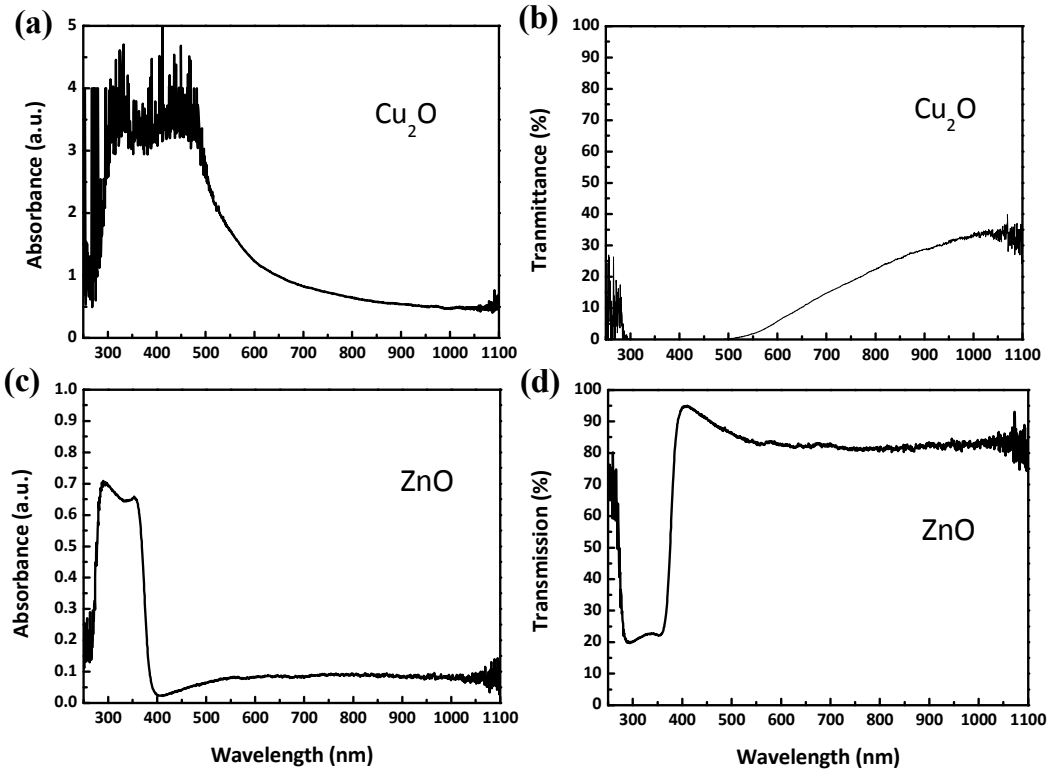

Figure 2. UV-vis absorbance and transmittance spectra: (a) absorbance and (b) transmittance of Cu_2O, (c) absorbance and (d) transmittance of ZnO.

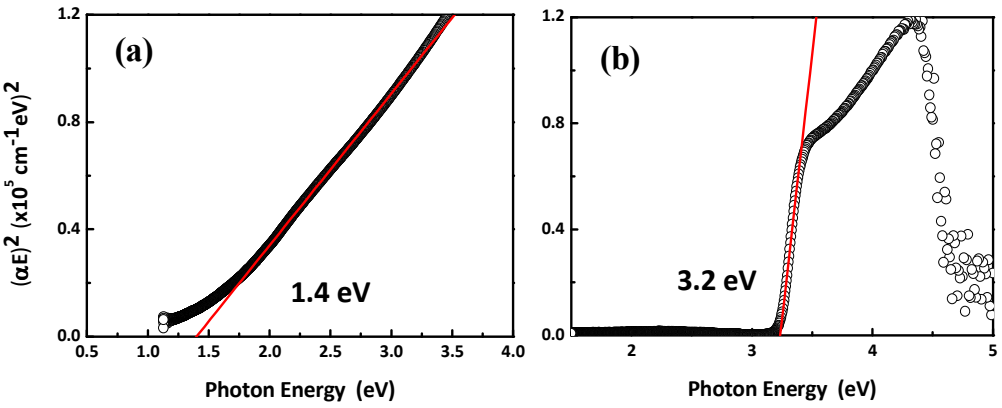

Figure 3. The extracted optical band gap of (a) Cu_2O and (b) ZnO from Tauc plot.

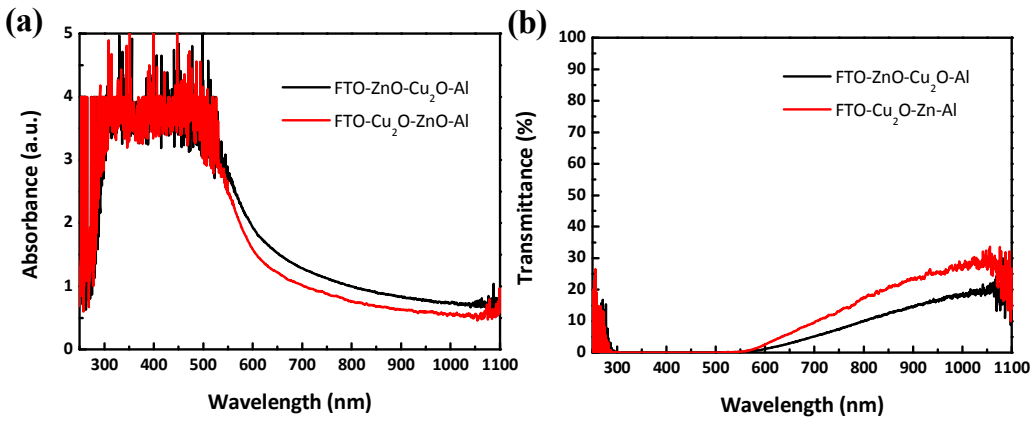

Figure 4. (a) Absorbance and (b) transmittance spectra of the whole stacks of FTO/ZnO/Cu_2O/Al and FTO/Cu_2O/ZnO/Al.

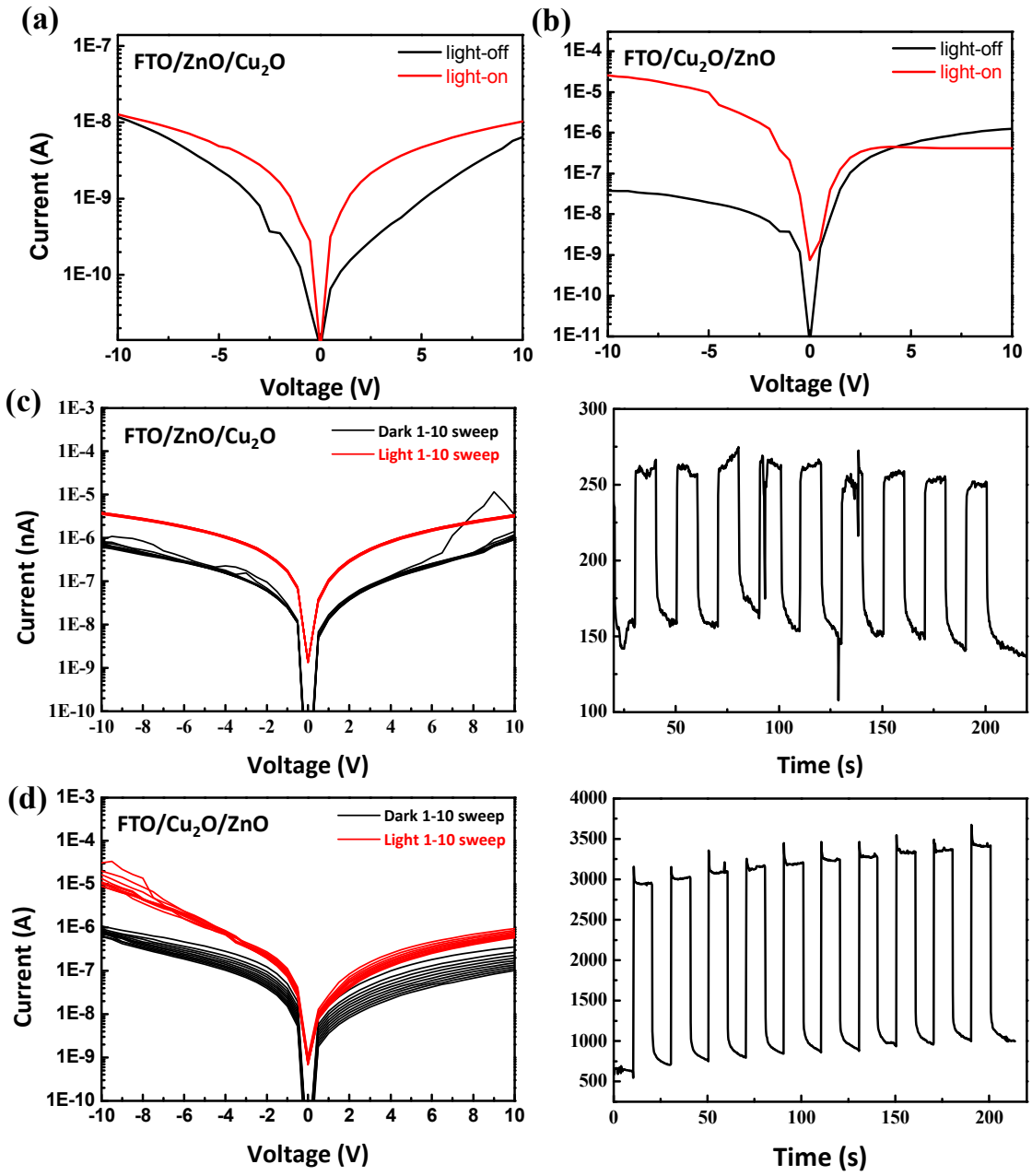

Figure 5. I-V characteristics of (a) FTO/ZnO/Cu_2O/Al and (b) FTO/Cu_2O/ZnO/Al under light-off (dark-current) and light-on (photo-current) condition. The repeated I-V (left) and I-t curves (right) of (c) FTO/ZnO/Cu_2O/Al and (d) FTO/Cu_2O/ZnO/Al.

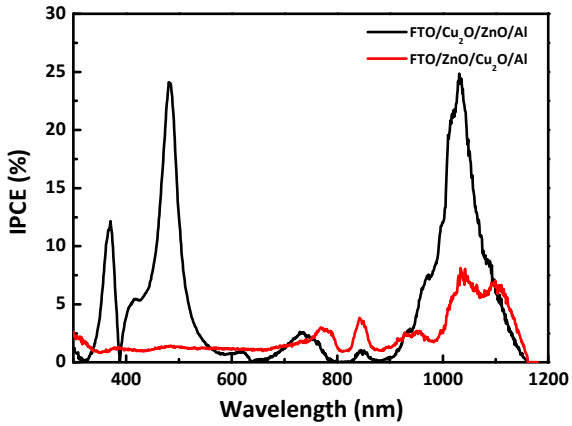

Figure 6. IPCE spectra of (red) FTO/ZnO/Cu_2O/Al and (black) FTO/Cu_2O/ZnO/Al.

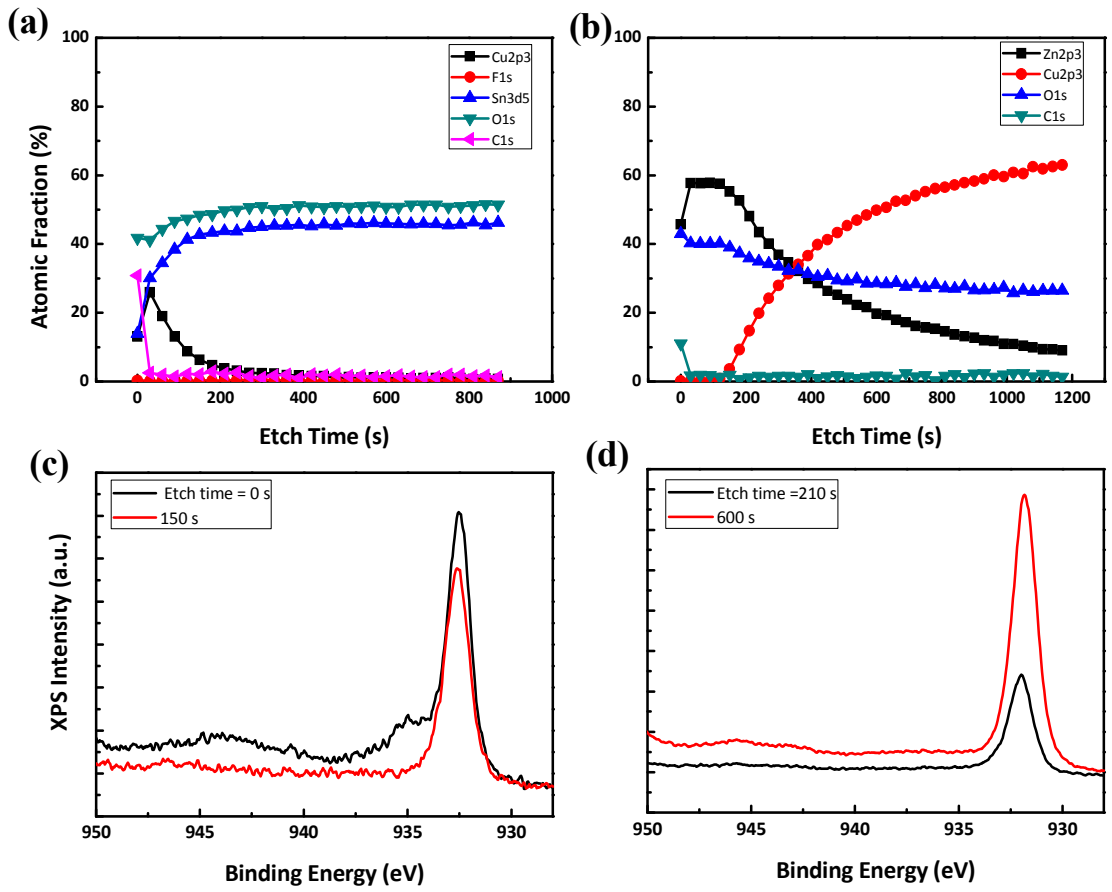

Figure 7. XPS depth profile of (a) FTO/Cu_2O atomic %, (b) ZnO/Cu_2O atomic % and Cu-2p narrow scan in the surface and bulk in (c) FTO/Cu_2O (etch time at 0 sec for surface and 150 sec for bulk) and (d) ZnO/Cu_2O (etch time at 210 sec for surface and 600 sec for bulk).

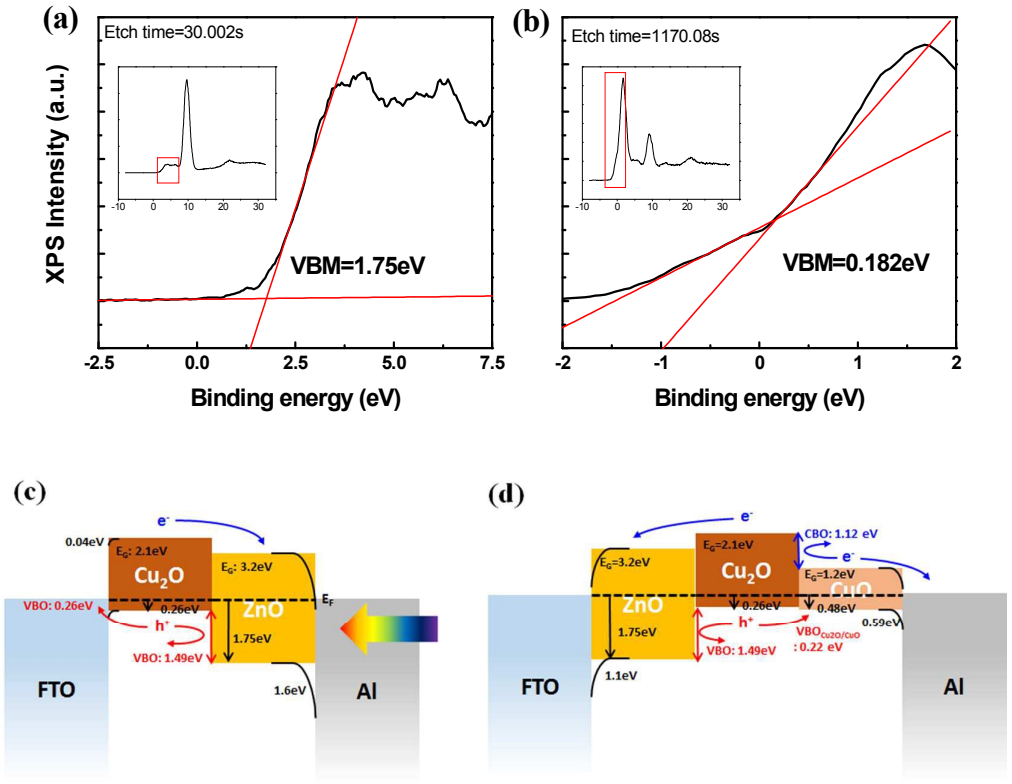

Figure 8. Valence band-edge XPS spectra with VBM values for (a) ZnO (at 30 sec of etch time) for and (b) Cu_2O (at 1170 sec of etch time) in FTO/Cu_2O/ZnO stack. The electronic band structure and alignment of (c) FTO/Cu_2O/ZnO/Al and (d) FTO/ZnO/Cu_2O/Al stacks. In FTO/Cu_2O/ZnO stack, there is no marked CBO and VBO to inhibit the charge separation at each interface. However, in FTO/ZnO/Cu_2O stack, hole transport toward FTO is blocked by the large VBO at ZnO/Cu_2O and CuO subphase present at Cu_2O surface leads to significantly different electronic band alignment from that in FTO/ZnO/Cu_2O.

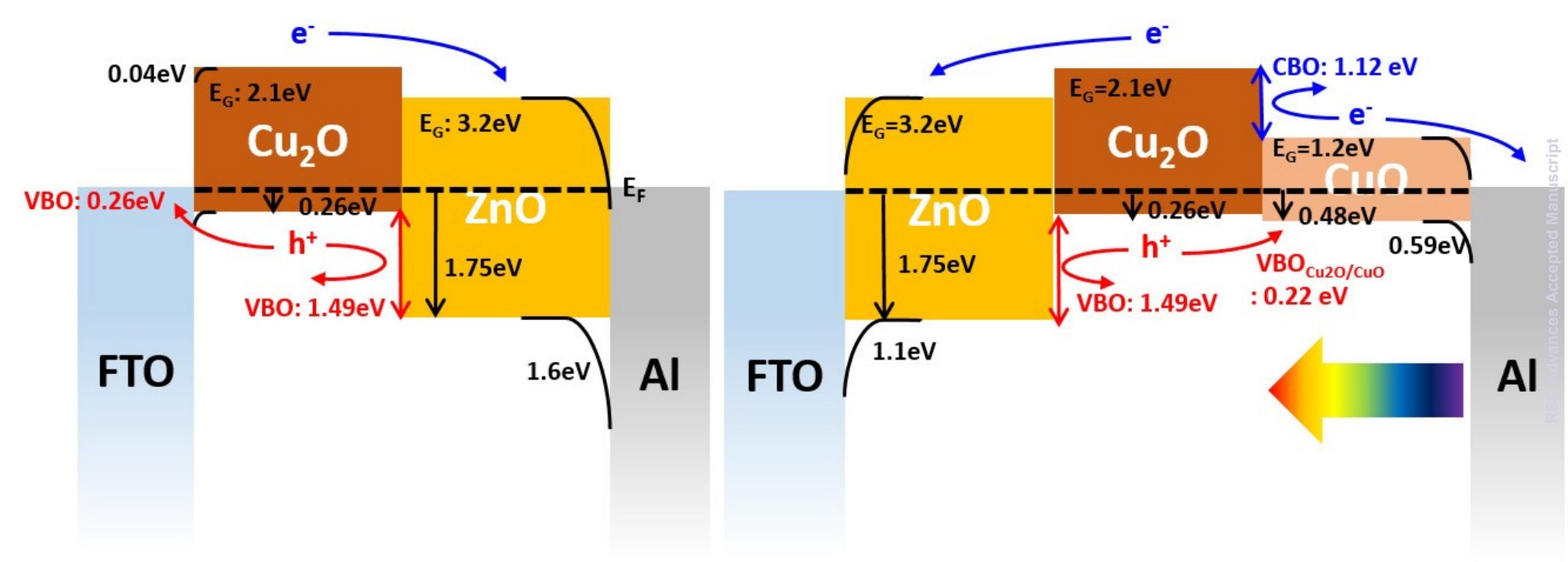
e-
0.04eV
E_G: 2.1eV
Cu2O
E_G: 3.2eV
E_F
VBO: 0.26eV
0.26eV
ZnO
h+
1.75eV
VBO: 1.49eV
FTO
1.6eV
Al
e-
CBO: 1.12 eV
E_G=2.1eV
E_G=3.2eV
Cu2O
e-
E_G=1.2eV
CuO
ZnO
0.26eV
0.48eV
0.59eV
h+
1.75eV
VBO_Cu2O/CuO
: 0.22 eV
VBO: 1.49eV
1.1eV
FTO
Al